Springer

Journal of
Mechanical
Science and
Technology

Journal of Mechanical Science and Technology 22 (2008) 1808~1820

www.springerlink.com/content/1738-494x
DOI 10.1007/s12206-008-0507-5

A numerical study of the fluid flow and heat transfer around a single row of tubes in a channel using immerse boundary method

Jaeeui Cho and Changmin Son*

Rolls-Royce plc, PO Box 31, Derby DE24 8BJ, England

(Manuscript Received March 7, 2008; Revised March 22, 2008; Accepted May 12, 2008)

Abstract

The analysis of the time-dependent and two-dimensional fluid flow and heat transfer around a single row of tubes in a channel is performed numerically. Due to its fundamental significance and practical importance, aerodynamic and heat transfer characteristics of tube bundle have been paid great attention by many researchers. In the present study, the immersed boundary method is applied by using a Cartesian grid system. Numerical solution for the governing equations of mass, momentum and energy conservation is obtained with the finite volume method. To validate the numerical approach with the immersed boundary method, the results have been compared with published data. The generation and evolution of vortical structures, wake interactions and their effects on the drag, lift and heat transfer are analyzed at different Reynolds numbers. The effect of hydraulic boundary layer development on the fluid flow and heat transfer is also investigated.

Keywords: Tube bundle; Time dependent numerical approach; Immerse boundary method

1. Introduction

The phenomenon of flow separation, bluff body wake and prediction of heat transfer from a single cylinder [1, 4, 12, 13, 14, 15, 17, 18, 22, 23, 25] and tube bundle [2, 3, 7, 19, 20, 24] has long been intensely studied because of its fundamental significance in flow physics and practical importance in aerodynamic and heat transfer applications.

Flow around a circular cylinder is well known to undergo a sequence of transition from steady to unsteady and from two- to three-dimensional phenomena with increasing Reynolds number. Each such transition has an attendant effect on overall heat transfer. Ahmad [1] conducted a numerical analysis of heat transfer by forced-convection from a horizontal stationary circular cylinder in a cross-flow of air by solving two-dimensional steady-state Navier-Stokes and energy equations in the Reynolds number range from 100 to 500. He suggested correlations for separation angle, drag coefficient, vorticity, pressure and Nusselt number as a function of Reynolds number. There have also been many other studies of flow past a circular cylinder, where the focus has been the investigation of flow transition from steady to unsteady and from two to three-dimensional phenomena [4, 12, 13, 14, 15, 17, 18, 22, 23, 25]. These studies have investigated the onset of three-dimensionality, the generation and evolution of vortical structures, wake transition due to three-dimensional instability and their effect on drag.

Complex wakes are found behind tube bundles in heat exchangers, fuel and control guide rods in nuclear reactors, piers and bridge pilings, oil and gas pipelines, cooling-tower arrays, suspension bridges and high-rise buildings. These complex wakes are usually formed by the interactions of a number of simple wakes generated by individual structures. Kang [7] investigated flows over two stationary cylinders in side-by-side arrangement at $40 \le \mathrm{Re} \le 160$ and with g less than

*Corresponding author. Tel.: +82 2 3476 7751
E-mail address: son.changmin@gmail.com

5 and classified six wake patterns in detail along with drag and lift coefficients, which are affected by gap spacing more than Reynolds number. Some numerical simulations for the fluid flow and heat transfer around tube bundles have been restricted to two-dimensional cases for the laminar flow [6, 19].

The present study is primarily concerned with complex flows and heat transfer in the laminar flow regime around a single row of tubes in a channel. The time-dependent numerical approach predicted the generation and evolution of vortical structures, wakes interactions, and their effects on the drag, lift and heat transfer in the range of 20 < Re < 180. The effects of wall boundary layer development on the distribution of flow and heat transfer are also discussed.

2. Computational details

Fig. 1 shows the computational domain in which the eight tubes are arranged in a row in the channel and its coordinate system. The immersed boundary method is used to simulate flow and thermal fields over a tube bundle in the channel. Therefore, the governing equations describing unsteady incompressible viscous flow and thermal fields in the present study are the momentum, continuity and energy equations:

$$\frac{\partial u_i}{\partial t}+\frac{\partial u_i u_j}{\partial x_j}=-\frac{\partial P}{\partial x_i}+\frac{1}{Re}\frac{\partial^2 u_i}{\partial x_j \partial x_j}+f \tag{1}$$

$$\frac{\partial u_i}{\partial x_i}-q=0 \tag{2}$$

$$\frac{\partial T}{\partial t}+\frac{\partial u_j T}{\partial x_j}=\frac{1}{RePr}\frac{\partial^2 T}{\partial x_j^2}+h \tag{3}$$

where x_i are Cartesian coordinates, u_i are the corresponding velocity components, t is the time, P is the pressure, and T is the temperature. The momentum forcing f and mass source/sink q are applied on the body surface or inside the body to satisfy the no-slip and mass conservation on the cell containing the immersed boundary. In Eq. (3), the heat source/sink h is applied to satisfy the iso-thermal boundary condition on the immersed boundary. All the variables are non-dimensionalized by the cylinder diameter D, inlet velocity U_i and the temperature difference between the cylinder surface temperature and inlet temperature $T_s - T_i$. The above non-dimensionalization results in two dimensionless parameters: $Re = U_i D/\upsilon$ and $Pr = \upsilon/\alpha$, where υ and α are the kinematic viscosity and thermal diffusivity. In the simulations to be reported here the Prandtl number, Pr, is a constant 0.71 corresponding to air.

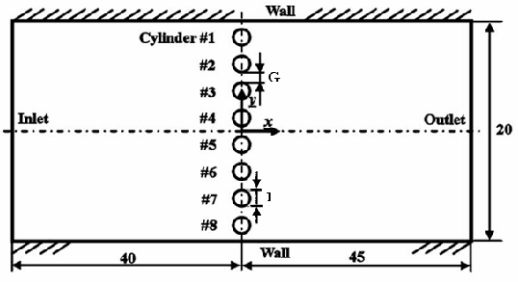

Fig. 1. Computational domain in which the eight tubes are arranged in a row in the channel and its coordinate system.

A two-step time-split scheme is used to advance the flow field. This scheme is based on the previous works of Kim and Moin [10] and Zang et al. [26]. First, the velocity is advanced from time level 'n' to an intermediate level '*' by solving the advection-diffusion equation without the pressure term. In the advection-diffusion step, the non-linear terms are treated explicitly by using the third-order Adams-Bashforth scheme. The diffusion terms are treated implicitly with the Crank-Nicolson scheme. Then, the Poisson equation for pressure, which is derived by using mass conservation, is solved fully implicitly. Once the pressure is obtained, the final divergence-free velocity field at 'n+1' is obtained with a pressure-correction step. The temperature field is advanced in a similar manner with the third-order Adams-Bashforth scheme for the advection term and the Crank-Nicolson scheme for the diffusion term. The central difference scheme with second-order accuracy based on the finite volume method is used for the spatial discretization. Additionally, a second-order linear, bilinear or trilinear interpolation scheme is applied to satisfy the no-slip and iso-thermal conditions on the immersed boundary. Further details of the immersed-boundary method are given in Kim et al. [9].

The size of computational domain is $-40 \le x \le 45$ and $-10 \le y \le 10$ for the streamwise and transverse directions, respectively, as shown in Fig. 1. The number of grids used is 575 and 1001 in the x and y directions, respectively, and the grid points around the cylinder are densely distributed with $\Delta x = \Delta y = 0.2$ as shown in Fig. 2. The condition of CFL≤0.3 is chosen to determine the non-dimensional time step used in the present calculation.

Table 1. Comparison of the present computational results for the time-averaged drag and lift coefficients, Strouhal number and Nusselt number with previous results.

Re		Present	Kim et al. [9]	Park et al. [16]	Williamson [21]	Kim & Choi [8]	Eckert & Soehngen [5]
40	C_D	1.520	-	1.510	-	-	-
	C_L'	-	-	-	-	-	-
	St	-	-	-	-	-	-
	Nu	3.293	-	-	-	3.230	3.480
100	C_D	1.340	1.330	1.330	-	-	-
	C_L'	0.330	-	0.332	-	-	-
	St	0.165	-	0.165	0.165	-	-
	Nu	5.218	-	-	-	5.130	5.230
120	C_D	1.332	1.510	1.320	-	-	-
	C_L'	0.396	0.320	0.410	-	-	-
	St	0.174	0.165	0.175	0.175	-	-
	Nu	5.684	-	-	-	5.620	5.690

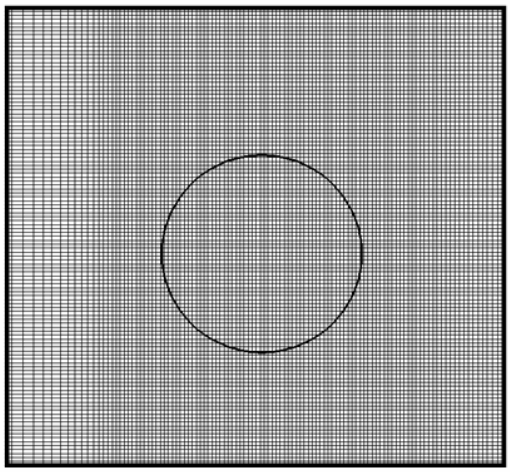

Fig. 2. Magnified view of grid system around a cylinder.

At the inflow and far-field boundaries, the Dirichlet boundary conditions, $u=1$, $v=0$ and $T=0$, are enforced. On the surfaces of the cylinder and channel boundary, no-slip and no-penetration boundary conditions, $u=0$ and $v=0$, are imposed for the velocity field, while an isothermal boundary condition, $T=1$, is enforced for the temperature. The convective boundary conditions, $\partial u_i/\partial t + c\partial u_i/\partial x = 0$ and $\partial T/\partial t + c\partial T/\partial x = 0$, are applied at the outflow boundary, where c is the space-averaged streamwise exit velocity, u and v are the velocity components in x and y directions, respectively.

Once the velocity and temperature fields are obtained, the local, time-averaged local, and time- and total surface-averaged Nusselt number, Nu, $\overline{Nu}$ and $\langle\overline{Nu}\rangle$, are defined as

$$Nu = \left.\frac{\partial T}{\partial n}\right|_{\text{wall}} \qquad \overline{Nu} = \frac{1}{t_P}\int_0^{t_P} Nu\,\mathrm{d}t$$

$$\langle\overline{Nu}\rangle = \frac{1}{D}\int_0^D \overline{Nu}\,\mathrm{d}S \tag{4}$$

where n is the normal direction to the walls and t_P is the period of time integration.

To check the validity of the present numerical method, we compared the present numerical results for the flow and heat transfer characteristics around a circular cylinder, two circular cylinders and a bundle of tubes in a row with those obtained by the previous researchers. The present numerical results for the drag coefficient, lift coefficient, Strouhal number and Nusselt number over a circular cylinder, for the drag and lift coefficients over two circular cylinders and for the streamwise and spanwise velocity profiles at 0.25D upstream from the centerline of the tubes represent very well the previous results [5, 6, 7, 8, 9, 16, 21] as shown in Table 1, Fig. 3 and Fig. 4, respectively.

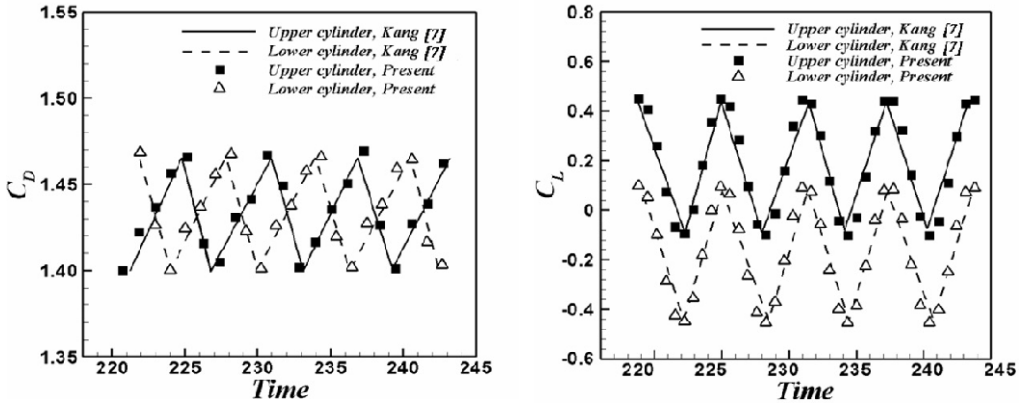

Fig. 3. Time evolutions of drag and lift coefficients around two cylinders at Re=100 and G=1.5.

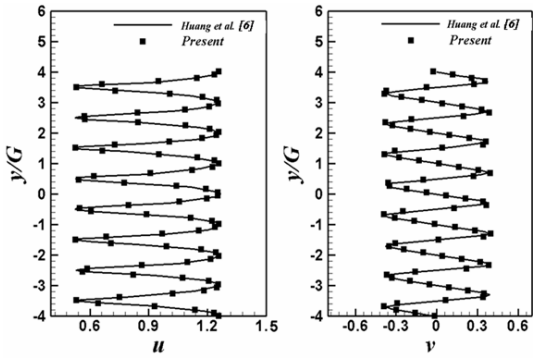

Fig. 4. Time-averaged streamwise and spanwise velocity profiles at 0.25 upstream of the centerline of the tubes.

3. Results and discussion

Fig. 5 shows the distribution of instantaneous spanwise vorticity contour for the flow past a bundle of tubes for different Reynolds numbers where the number of tubes arranged in a single row is eight and the gap G between the tubes is 1.5. When the Reynolds number is 20 and 40, the flow is steady. There are no flow interactions among the tubes from #2 to #7, hence the flows around tubes from #2 to #7 are similar to the flow around a single tube. However, we can observe some interactions between the top wall and #1 cylinder and between the bottom wall and #8 cylinder which are caused by the development of wall boundary layer due to the presence of top and bottom walls. When $Re \geq 60$, the flow around a bundle of tubes becomes time-dependent and we can observe the vortex shedding resulting in the formation of complex flow patter in the wake. We can observe some interactions between the vortices in the wake without any mixing between them at the region of $0 \leq x \leq 4.5$ but with strong mixing at the region of $x > 4.5$. As the Reynolds number increases, the fields of instantaneous vortices in the wake are divided into the smaller scale as the flow moves downstream. When $Re = 60$, the fields of instantaneous vortices in the wake converges into the center as the flow moves downstream. As the Reynolds number increases, the fields of instantaneous vortices in the wake spread out in the channel because the effect of mixing increases. As a result, the fields of instantaneous vortices at $Re = 180$ are distributed widely in the whole region of wake.

Fig. 6 shows the distribution of time-averaged skin friction $\overline{C}_f$ at the bottom wall for different Reynolds numbers. At the upstream of a bundle of tubes, the time-averaged skin friction decreases with increasing Reynolds number because the thickness of the hydraulic boundary layer decreases as the Reynolds number increases. In the region close to the center of a bundle of tubes, the time-averaged skin friction increases very rapidly because the velocity through the small gap between the bottom wall and #8 cylinder increases rapidly. When $Re \geq 100$, the time-averaged skin friction coefficient has negative values at the location just close to rear stagnation point of tubes, meaning that the re-circulating flow is formed on the lower wall after the flow passes through the gap between the lower wall and #8 cylinder. At the downstream of tube bundle, the variation of time-averaged skin friction for different Reynolds numbers is small.

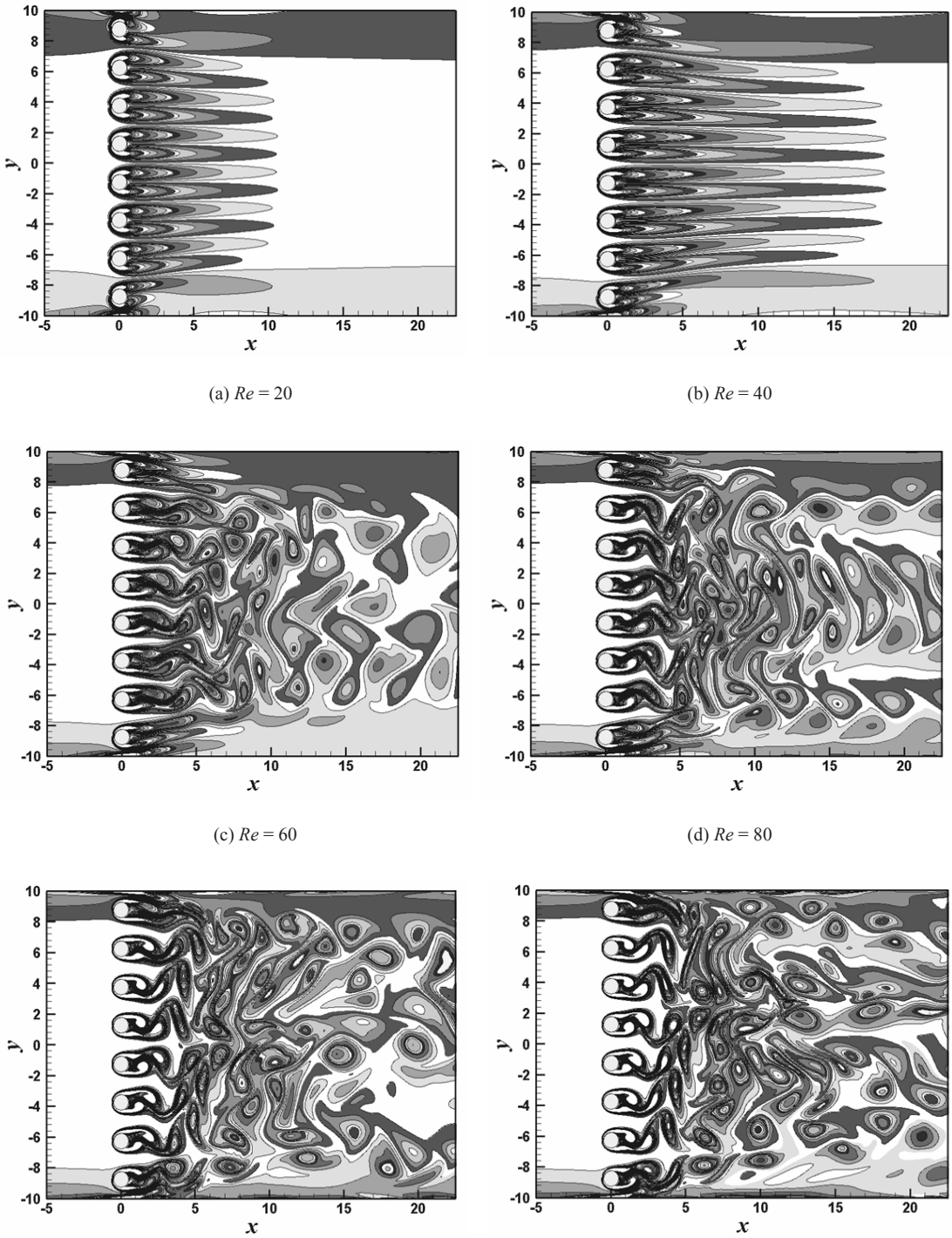

(a) Re = 20 (b) Re = 40

(c) Re = 60 (d) Re = 80

(e) Re = 100 (f) Re = 120

Fig. 5. Distribution of instantaneous spanwise vorticity contour for the flow past a bundle of tubes for different Reynolds numbers when G =1.5.

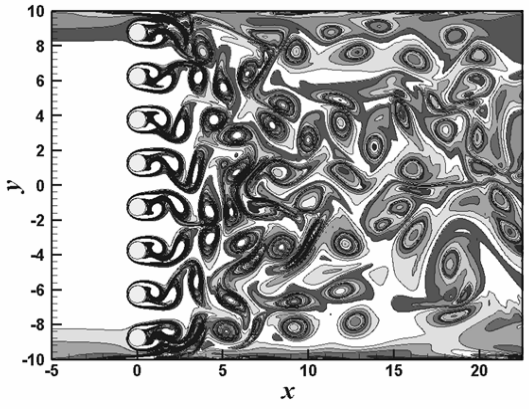

(g) *Re* =140

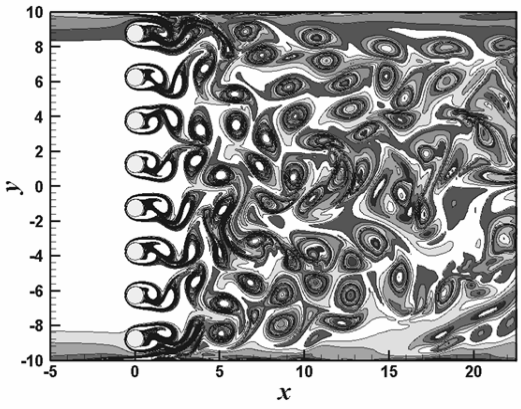

(h) *Re* = 160

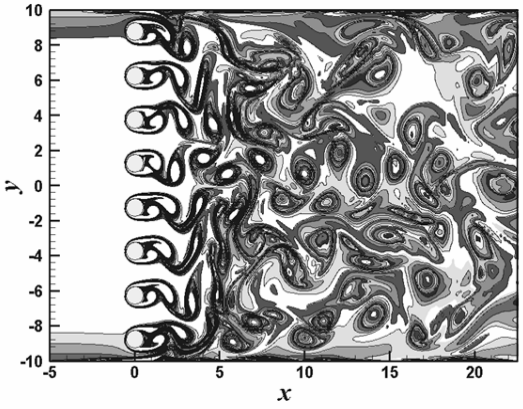

(i) *Re* = 180

Fig. 5. Distribution of instantaneous spanwise vorticity contour for the flow past a bundle of tubes for different Reynolds numbers when *G*=1.5 (Continued).

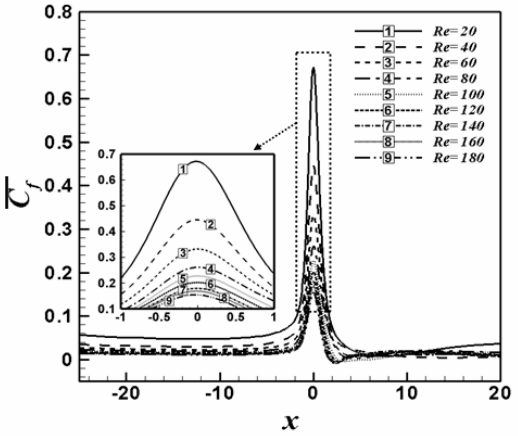

Fig. 6. Distribution of time-averaged skin friction at the bottom wall for different Reynolds numbers.

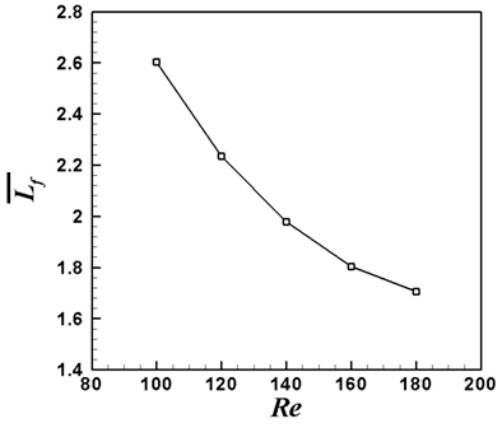

Fig. 7. Time-averaged length of re-circulating bubble formed on the lower wall as a function of Reynolds number.

Fig. 7 shows the time-averaged length of re-circulating bubble, $\overline{L}_F$, formed on the lower wall as a function of Reynolds number. Here $\overline{L}_F$ is defined as the length from the rear stagnation point of tubes to the end of re-circulating bubble along the flow direction on the lower wall. The time-averaged re-circulating flow on the lower wall is formed when $Re \geq 100$ as it is already mentioned. $\overline{L}_F$ decreases as the Reynolds number increases at $Re \geq 100$ because the vortex shedding caused by the shear layer instability moves upstream along the tube surface with increasing Reynolds number as the flow passes through a bundle of tubes.

Fig. 8 shows the distribution of time-averaged streamwise velocity $\overline{u}$ for different Reynolds numbers at different streamwise locations. Fig. 8(a) shows the distribution of time-averaged streamwise velocity at $x = -10$ which is far upstream from a bundle of tubes. The presence of a bundle of tubes in the channel does not give any effects on the distribution of time-averaged streamwise velocity at $x = -10$, hence shows the characteristics of typical channel flow. As the Reynolds number increases, the time-averaged streamwise velocity at the viscous layer close to the wall increases due to the decreasing thickness of the hydraulic boundary layer. However, the time-averaged streamwise velocity at the potential core of the channel decreases in order to satisfy the continuity equation with increasing Reynolds number.

Fig. 8(b) shows the distribution of time-averaged streamwise velocity at $x = -1.5$ which is near upstream from a bundle of tubes. The presence of a

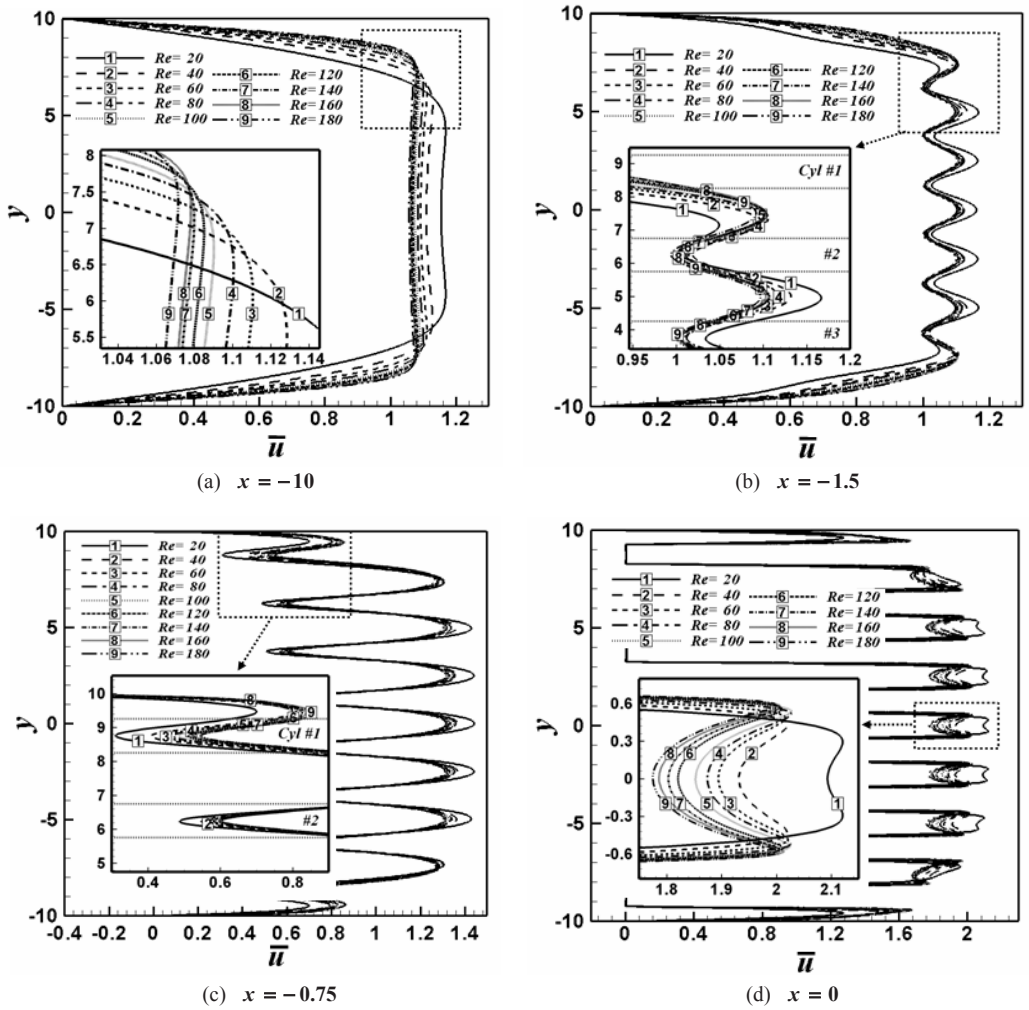

(a) $x = -10$ (b) $x = -1.5$

(c) $x = -0.75$ (d) $x = 0$

Fig. 8. Distribution of time-averaged streamwise velocity for different Reynolds numbers at different streamwise locations.

bundle of tubes gives some effects on the distribution of time-averaged streamwise velocity at $x=-1.5$. Thus the distribution of time-averaged streamwise velocity at $x=-1.5$ is different from that at $x=-10$. At $x=-1.5$, the time-averaged streamwise velocity in front of a bundle of tubes (from #2 to # 7 cylinders) decreases due to the flow deceleration caused by the presence of a bundle of tubes, whereas the time-averaged streamwise velocity between tubes increases due to the flow acceleration caused by the decrease in the cross-sectional area, compared to the time-averaged streamwise velocity at $x=-10$. At the regions both from the top wall to #1 cylinder and from the bottom wall to #8 cylinder, the effect of hydraulic boundary layer development is larger than the presence of tubes, and as a result the time-averaged streamwise velocity at $x=-1.5$ is similar to that at $x=-10$. As the Reynolds number increases at $x=-1.5$, the time-averaged streamwise velocity at the viscous layer close to the wall increases, whereas that at the potential core of the channel decreases, similar to the distribution of the time-averaged streamwise velocity at $x=-10$.

Fig. 8(c) shows the distribution of time-averaged streamwise velocity at $x=-0.75$ which is closer to a bundle of tubes than at $x=-1.5$. As the flow approaches a bundle of tubes, the flow at $x=-0.75$ accelerates more between tubes and decelerates more in front of tubes (from #1 to #8 cylinder), compared to those at $x=-1.5$. Thus, the variation of the time-averaged streamwise velocity at the potential core at $x=-0.75$ is larger than that at $x=-1.5$. The maximum values of the time-averaged streamwise velocity between tubes at $x=-0.75$ are larger than that at $x=-1.5$, whereas the minimum values of the time-averaged streamwise velocity in front of tubes at $x=-0.75$ are smaller than that at $x=-1.5$. As the Reynolds number increases at $x=-0.75$, the time-averaged streamwise velocity decreases between tubes and increases in front of tubes. As the flow approaches more a bundle of tubes from $x=-1.5$ to $x=-0.75$, the presence of #1 and #8 cylinders on the time-averaged streamwise velocity gives more effects on the time-averaged streamwise velocity than the development of hydraulic boundary layer, and as a result the time-averaged streamwise velocity in front of # 1 and #8 cylinders at $x=-0.75$ decreases due to the flow deceleration in the presence of #1 and #8 cylinders, unlikely to the time-averaged streamwise velocity in front of #1 and #8 cylinders at $x=-1.5$.

Fig. 8(d) shows the distribution of time-averaged streamwise velocity at $x=0$ which is the centerline of the tubes. The magnitude of time-averaged streamwise velocity between tubes at $x=0$ is about two times larger than the inlet velocity of channel, which is larger than that at $x=-0.75$, -1.5 and -10. As the Reynolds number increases, the time-averaged streamwise velocity between tubes at $x=0$ decreases with a concave shape, unlikely to the convex shape of the time-averaged streamwise velocity at $x=-0.75$ and -1.5, due to the viscous effect around the cylinder surface. The distribution of time-averaged streamwise velocity between the top wall and #1 cylinder at $x=0$ is generally similar to that at $x=-0.75$.

Fig. 9 shows the distribution of time-averaged front stagnation point along the upper and lower surfaces of eight cylinders for different Reynolds numbers. The angle along the upper cylinder surface is defined as positive, whereas the angle along the lower cylinder surface is defined as negative. Because the #1 cylinder is close to the top wall, the flow around #1 cylinder is affected by the hydraulic boundary layer development due to the presence of channel walls. Thus, the flow velocity along the upper surface of #1 cylinder is lower than that along the lower surface of #1 cylinder. As a result, the front stagnation point of #1 cylinder has a negative value, as shown in the time-averaged streamline around #1 and #8 cylinders in Fig. 10. Similar to the case of #1 cylinder, the flow velocities along the upper surfaces of #2 and #3 cylinders are also lower than those along the lower surfaces of #2 and #3 cylinders. As a result, the front stagnation points of #2 and #3 cylinders have negative values. Moving from the top wall to the centerline of the channel ($y=0$), the absolute value of front stagnation point decreases because the difference in the magnitude of flow velocities along the upper and lower cylinder surfaces decreases with decreasing effect of hydraulic boundary layer development. For the case of #4 cylinder, the magnitude of flow velocity along the upper surface of #4 cylinder is the same as that along the lower surface of #4 cylinder, resulting in zero front stagnation point. As the Reynolds number increases, the absolute value of front stagnation point for the #1 ~ #4 cylinders decreases because the inertia effect increases and the difference in the magnitude of flow velocities along the upper and lower surfaces of cylinders decreases. The front stagnation points for the #5 ~ #8 are sym-

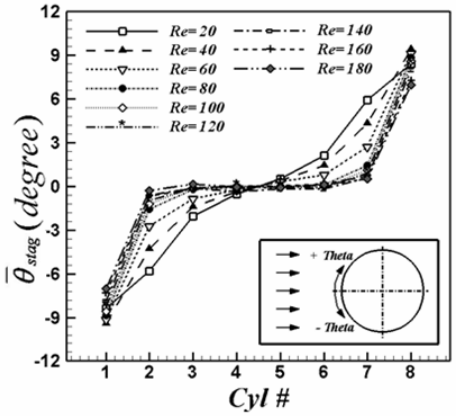

Fig. 9. Distribution of time-averaged front stagnation point along the surfaces of eight cylinders for different Reynolds numbers.

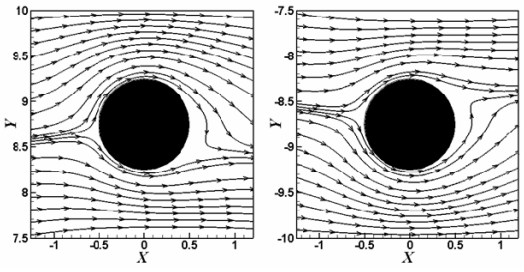

(a) #1 cylinder (b) # 8 cylinder

Fig. 10. Time-averaged streamlines around #1 and #8 cylinders.

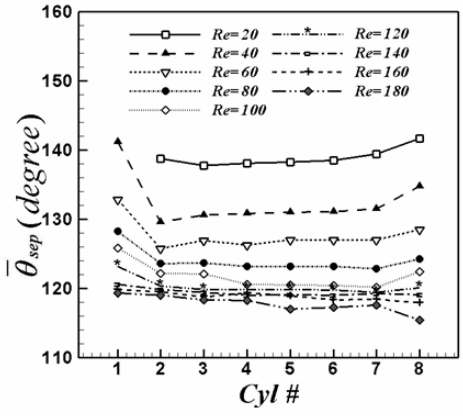

(a) Upper surfaces of cylinders

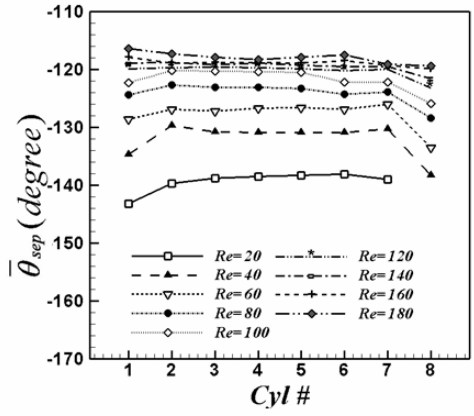

(b) Lower surfaces of cylinders

Fig. 11. Distribution of time-averaged separation point at the upper and lower surfaces of eight cylinders for different Reynolds.

metric to those for the #1 ~ #4 cylinders with positive values.

Fig. 11 shows the distribution of time-averaged separation point at the upper and lower surfaces of eight cylinders for different Reynolds numbers. When $Re = 20$, there are no flow separations at the upper surface of #1 cylinder and at the lower surface of #8 cylinder. As the Reynolds number increases, the flow separation point moves upstream along the lower and upper surfaces of cylinders, and as a result the absolute value of flow separation point for different cylinders decreases. The absolute values of flow separation points for the #1 (#8) cylinder are lower than those for other cylinders due to the effect of hydraulic boundary layer in the presence of top and bottom walls at the specified Reynolds number. The variation of flow separation points for the #2 ~ #7 cylinders at the specified Reynolds number is small.

Fig. 12 shows the time-averaged drag coefficient around eight cylinders as a function of Reynolds number. The drag coefficient decreases with increasing Reynolds number. The drag coefficient of #1 cylinder is lower than the drag coefficients of #2, #3 and #4 cylinders, because the flow velocity around the #1 cylinder is lower than that around #2, #3 and #4 cylinders due to the hydraulic boundary layer development in the presence of wall. As we move form the #1 cylinder to the #4 cylinder, the drag coefficient increases with decreasing effect of hydraulic boundary layer in the presence of wall. The drag coefficients of #1, #2 and #3 cylinders are 28.7%, 6.1% and 1.4% lower than the drag coefficient of #4 cylinder. The distribution of drag coefficients of #5, #6, #7 and #8 cylinders as a function of Reynolds number is the same as that of #4, #3, #2 and #1 cylinders, respectively, because the distribution of time-averaged flow

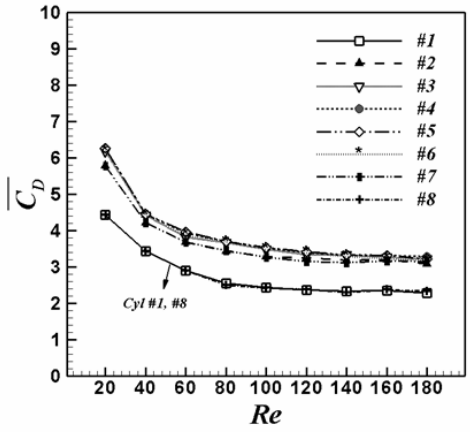

Fig. 12. Time-averaged drag coefficient around eight cylinders as a function of Reynolds number.

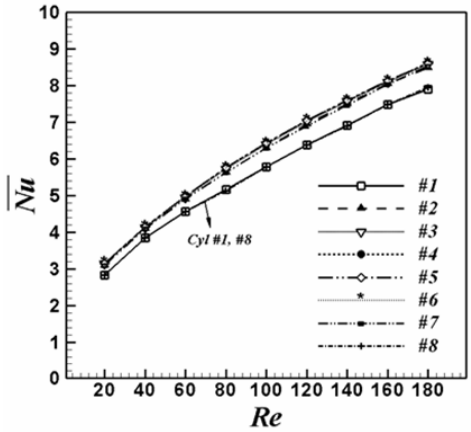

Fig. 14. Time- and surface-averaged Nusselt number as a function of Reynolds numbers for different Reynolds numbers.

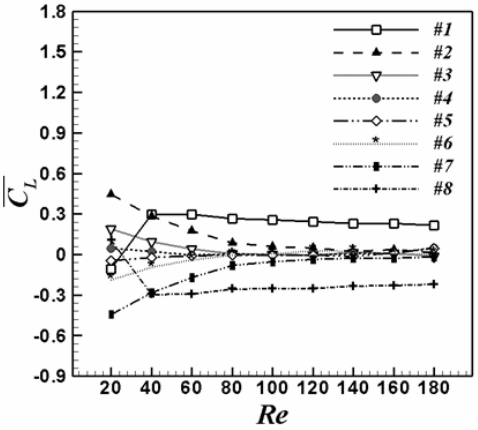

Fig. 13. Time-averaged lift coefficient around eight cylinders as a function of Reynolds number.

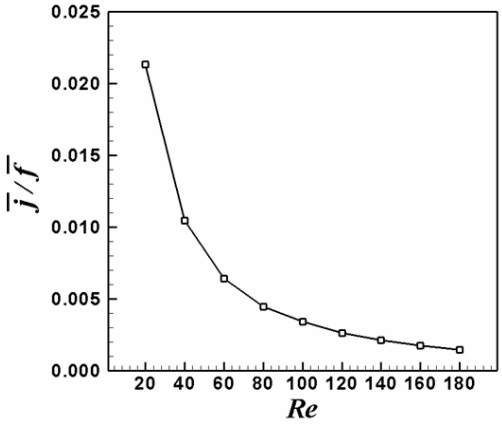

Fig. 15. Time- and area-averaged goodness factor $\overline{j}/\overline{f}$ as a function of Reynolds number.

is symmetric around the centerline of the channel ($y = 0$) as shown in Fig. 8.

Fig. 13 shows the time-averaged lift coefficient around eight cylinders as a function of Reynolds number. As it is mentioned above, the flow velocity around #1 cylinder is affected by the hydraulic boundary layer development in the presence of a wall. Thus, the lift coefficients of #1 cylinder have positive values when $Re \geq 40$ because the flow velocity along the upper surface of #1 cylinder is larger than that along the lower surface of #1 cylinder. However, when $Re = 20$, the flow velocity along the upper surface of #1 cylinder is lower than that along the lower surface of #1 cylinder; as a result the lift coefficient of #1 cylinder has a negative value. As we move from the top wall to the centerline of the channel, the difference in the flow velocities along the upper and lower cylinder surfaces, resulting in the decrease of the time-averaged lift coefficient. As the Reynolds number increases, the time-averaged-lift coefficient of #2, #3 and #4 cylinders approaches the zero value, meaning that the flow velocities along the upper cylinder surfaces are almost the same as those along the lower cylinder surfaces. The time-averaged lift coefficient for the #5, #6 and #7 cylinders as a function of Reynolds number has the same absolute magnitude with the opposite sign to those for the #4, #3 and #2 cylinders, respectively, because the distribution of flow velocity is symmetric to the centerline of the channel.

Fig. 14 shows the time- and surface-averaged Nusselt number as a function of Reynolds numbers for

different Reynolds numbers. As the Reynolds numberincreases, the time- and surface-averaged Nusselt number increases with increasing convection effects on the heat transfer from a bundle of tubes. The time- and surface-averaged Nusselt numbers of #1, #2 and #3 cylinders are 8.9%, 1.54% and 0.34%, respectively, lower than the Nusselt number of the # 1 cylinder. So the difference in the time- and surface-averaged Nusselt number among the #2, #3 and #4 cylinders is small, compared to the large difference of time- and surface-averaged Nusselt number for the case of #1 cylinder due to the effect of hydraulic boundary layer development in the presence of wall. Similar to the flow and time-averaged drag coefficient, the time- and surface-averaged Nusselt number for the #5, #6, #7 and #8 cylinders as a function of Reynolds number is the same as that for the #4, #3, #2 and #1 cylinders.

Fig. 15 shows the time- and area-averaged goodness factor $\overline{j}/\overline{f}$ as a function of Reynolds number. The $\overline{j}/\overline{f}$ decreases nonlinearly with increasing Reynolds number and can be expressed as.

$$\overline{j}/\overline{f} = 4.438Re^{-1.5} + 11.316Re^{-2} \quad (5)$$

This expression shows that the pressure drop is larger than the increase of heat transfer.

4. Conclusions

The fluid flow and heat transfer around a single row of eight tubes are investigated by using the finite volume method applying an immersed boundary approach.

(1) The successful validation against published data confirms that the immerse boundary approach can be applied to complicated flow and heat transfer field.
(2) The presence of top and bottom walls gives some effects on the flow around a bundle of tubes because of the hydraulic boundary layer development from the top and bottom walls. The front stagnation points of #1, #2, #3 and #4 cylinders are located at the lower surface of cylinders, whereas those of #5, #6, #7 and #8 cylinders are at the upper surface of cylinders. As we move from top and bottom walls to the centerline of channel, the front stagnation points move to the horizontal centerline of cylinders because the difference in the magnitude of flow velocities along the upper and lower cylinders surfaces decreases.
(3) The separation point moves upstream along the surface of cylinders as the Reynolds number increases. When the Reynolds number is 20, there are no flow separations along the upper surface of #1 cylinder and along the lower surface of #8 cylinder.
(4) As the Reynolds number increases, the time-averaged drag coefficient and the time- and surface-averaged Nusselt number decrease. As we move from the top and bottom walls to the centerline of channel, the time-averaged drag coefficient and time- and surface-averaged Nusselt number increase because the effect of the presence of walls to the fluid flow and heat transfer around cylinders decreases.
(5) The time-averaged lift coefficients for the #1 and #8 cylinders have some positive and negative values as the Reynolds number increases because the flow velocities along the upper surface of #1 and #8 cylinders are different from those along the lower surfaces of #1 and #8 cylinders. However, as we move from the walls to the centerline of channel, the time-averaged lift coefficient around #2, # and #4 (#5, #6 and #7) approaches to zero because the difference in the flow velocities along the upper and lower cylinder surfaces decreases.
(6) The derived correlation for the time- and area-averaged goodness factor $\overline{j}/\overline{f}$ as a function of Reynolds number is $\overline{j}/\overline{f} = 4.438Re^{-1.5} + 11.316Re^{-2}$

Nomenclature

c : Dimensionless space-averaged streamwise exit velocity
C_D : Drag coefficient
$\overline{C}_f$: Time-averaged skin friction
C_L : Lift coefficient
D : Tube diameter
f : Momentum forcing or friction factor
G : Dimensionless gap between tubes
g : Gravity
h : Heat source or sink
$\overline{j}$: Time-averaged Colburn j factor
$\overline{L}_f$: Time-averaged length of recirculation bubble
n : Normal direction to the wall
Nu : Local Nusselt number
$\overline{Nu}$: Time-averaged local Nusselt number

$\langle Nu \rangle$: Time- and surface-averaged Nusselt number
P : Dimensionless pressure
Pr : Prandtl number
q : Mass source or sink
Re : Reynolds number
t : Dimensionless time
T : Dimensionless temperature
u_i : Dimensionless velocity tensor in i direction
u , v : Velocity components in x and y directions
x_i : Dimensionless Cartesian coordinate tensor
x , y : Cartesian coordinates in the x and y directions

Greek symbols

α : Thermal diffusivity
θ : Angle
υ : Kinematic viscosity

Sub/Superscripts

i : Coordinates, inlet
j : Coordinates
s : Surface
sep : Separation
$stag$: Stagnation

References

[1] R. A. Ahmad, Steady-state numerical solution of the Navier-Stokes and energy equations around a horizontal cylinder at moderate Reynolds numbers from 100 to 500, *Heat Transfer Eng.* 17 (1) (1996) 31-80.

[2] H. R. Barsamian and Y. A. Hassan, Large eddy simulation of turbulent cross flow in tube bundles, *Nucl. Eng. Design* 172 (1997) 103-122.

[3] S. B. Beale and D. B. Spalding, A numerical study of unsteady flow in in-line and staggered tube banks, *J. Fluid. Struct.* 13 (1999) 723-754.

[4] M. Braza, P. Chassaing and H. H. Minh, Numerical study and physical analysis of the pressure and velocity fields in the near wake of a circular cylinder, *J. Fluid Mech.* 165 (1986) 79-130.

[5] E. R. G. Eckert and E. Soehngen, Distribution of heat transfer coefficients around circular cylinders, *Trans. ASME* 75 (1952) 343-347.

[6] Z. Huang, J. A. Olson, R. J. Kerekes and S. I. Gree, Numerical simulation of the flow around rows of cylinders, *J. Comput. Fluids* 35 (2006) 485-491.

[7] S. Kang, Characteristics of flow over two circular cylinders in a side-by-side arrangement at low Reynolds numbers, *Phys. Fluids* 19 (9) (2003) 2486-2498.

[8] J. W. Kim and H. Choi, An immersed boundary finite volume method for simulation of heat transfer in complex geometries, *KSME Int. J.* 18 (6) (2004) 1026-1035.

[9] J. Kim, D. Kim and H. Choi, An immersed boundary finite-volume method for simulations of flow in complex geometries, *J. Comput. Phys.* 171 (2001) 132-150.

[10] J. Kim and P. Moin, Application of a fractional-step method to incompressible Navier-Stokes Equation, *J. Comput. Phys. 59 (1985)* 308-323.

[11] Y. T. Krishne Gowda, B. S. V. P. Patnaik, P. A. Aswatha Narayana and K. N. Seetharamu, Finite element simulation of transient laminar flow and heat transfer past an in-line bank, *Int. J. Heat Fluid Flow* 19 (1998) 49-55.

[12] G. Karniadakis and G. S. Triantafyllou, Three-dimensional dynamics and transition to turbulence in the wake of bluff objects, *J. Fluid Mech.* 238 (1992) 1-30.

[13] A. G. Kravchenko and P. Moin, Numerical studies of flow over a circular cylinder at $Re_D = 3900$, *Phys. Fluids* 12 (2) (2000) 403-417.

[14] R. Mittal and S. Balachandar, Direct numerical simulation of flow past elliptic cylinders, *J. Comput. Phys.* 124 (1994) 351-367.

[15] R. Mittal and S. Balachandar, Generation of streamwise vortical structures in bluff body wakes, *Phys. Review Letters* 75 (8) (1995) 1300-1302.

[16] J. Y. Park, K. Y. Kwon and H. Choi, Numerical solutions of flow past a circular cylinder at Reynolds numbers up to 160, *KSME Int. J.* 12 (6) (1998) 1200-1205.

[17] T. Tamura and I. Ohta, On the reliability of two-dimensional simulation for unsteady flows around a circular-type structure, *J. Wind Eng. and Industrial Aero.* 35 (1990) 275-298.

[18] M. Thompson, K. Hourigan and J. Sheridan, Three-dimensional instabilities in the wake of a circular cylinder, *Exp. Therm. Fluid Sci.* 12 (1996) 190-196.

[19] Y. Q. Wang, L. A. Penner and S. J. Ormiston, Analysis of laminar forced convection of air for crossflow in banks of staggered tubes, *Numer. Heat Trans. A* 38 (2000) 819-845.

[20] J. K. Watterson, W. N. Dawes, A. M. Savil and A. J. White, Predicting turbulent flow in a staggered

tube bundle, *Int. J. Heat. Fluid Flow* 20 (1999) 581-591.

[21] C. H. K. Williams, Evolution of a single wake behind a pair of bluff bodies, *J. Fluid Mech.* 159 (1985) 1-18.

[22] C. H. K. Williamson, Three-dimensional wake transition, *J. Fluid Mech.* 328 (1996a) 345-407.

[23] C. H. K. Williamson, Vortex dynamics in the cylinder wake, *Annual Rev. Fluid Mech.* 28 (1996b) 477-543.

[24] A. S. Wilson and M. K. Bassiouny, Modeling of heat transfer for flow across tube banks, *Chemical Engineering and Processing* 39 (2000) 1-14.

[25] J. Zhang, C. Dalton, A three-dimensional simulation of a steady approach flow past a circular cylinder at low Reynolds number, *Int. J. Numer. Meth. Fluids* 26 (1998) 1003-1022.

[26] Y. Zang, R. L. Street and J. R. Koseff, A non-staggered grid, fractional step method for time-dependent incompressible Navier–Stokes equations in curvilinear coordinates, *J. Comput. Phys.* 114 (1994) 18–33.